



Evaluating the effects of spatial resolution on hyperspectral fire detection and temperature retrieval

D. Scott Matheson, Philip E. Dennison*

Department of Geography and Center for Natural and Technological Hazards, 260 S Central Campus Dr, Room 270, Salt Lake City, UT 84112, University of Utah, United States

ARTICLE INFO

Article history:

Received 6 July 2011

Received in revised form 26 June 2012

Accepted 27 June 2012

Available online xxxx

Keywords:

Imaging spectrometer

Wildfire

Multiple endmember spectral mixture analysis (MESMA)

Hyperspectral fire detection index (HFDI)

AVIRIS

HyspIRI

ABSTRACT

Hyperspectral data covering a wavelength range of 1.2–2.5 μm can be used to detect fires and model fire temperature and background land cover. Previous work has used hyperspectral data acquired from airborne platforms, limiting spatial resolution to finer than 20 m. The Hyperspectral InfraRed Imager (HyspIRI), a proposed hyperspectral/thermal infrared mission, will provide hyperspectral data over a spectral range of 0.35–2.5 μm at a spatial resolution of 60 m. This study uses airborne hyperspectral data to investigate changes in modeled fire temperature and area as spatial resolution is varied from 5 m to coarser than 60 m. Four images containing active fires were acquired by the Airborne Visible Infrared Imaging Spectrometer (AVIRIS), with spatial resolutions ranging from ~5 to ~20 m. Gaussian and aggregation resampling methods were compared for one scene containing fire, and both resampling methods were found to produce similar radiance values. As spatial resolution coarsened, the area flagged as having fire by the hyperspectral fire detection index (HFDI) increased. Fire temperature modeled using a multiple endmember spectral mixing model decreased at coarser spatial resolutions, while the modeled fire fractional area increased. Coarser spatial resolution hyperspectral data, including data collected by HyspIRI, are likely to provide increased fire area and lower temperatures when compared against simultaneously acquired higher spatial resolution data. Saturation in shortwave infrared (SWIR) bands was found in all four images, and increasing SWIR saturation thresholds could lead to improvements in fire characterization.

© 2012 Elsevier Inc. All rights reserved.

1. Introduction

Wildfire is a globally important process, affecting a wide variety of ecosystems and often endangering human life and settlement. The impacts of wildfires add to growing concerns regarding atmospheric pollutants, the carbon cycle and global climate change. Remote sensing has appropriately become an essential tool for examining and evaluating the effects of wildfires on the environment due to its ability to map fires and fire impacts over large areas (Lentile et al., 2006). Measurement of reflected and emitted shortwave electromagnetic radiation at high spectral resolutions can provide valuable information on fuels (Dennison et al., 2003; Varga & Asner, 2008), active fires (Dennison & Matheson, 2011; Dennison et al., 2006) and the impacts of fire on vegetation and soils (Kokaly et al., 2007; Lewis et al., 2007). Although remotely sensed information represents a snapshot in time, repeat acquisitions can allow detection of change over time, such as the regeneration of vegetation in a burned area (Riaño et al., 2002).

Hyperspectral sensors utilize a large number of contiguous bands, each with a narrow wavelength range (typically ≤ 10 nm). Previous work using Airborne Visible Infrared Imaging Spectrometer (AVIRIS)

data has demonstrated that hyperspectral data can be used to detect fire (Dennison & Roberts, 2009) and model fire temperature (Dennison & Matheson, 2011; Dennison et al., 2006). Yet AVIRIS, like all airborne sensors, faces issues of varying spatial resolutions and has limited spatial and temporal coverage. The National Research Council Decadal Survey on NASA Earth Science Applications recommended the development of a hyperspectral/thermal infrared satellite mission (National Research Council, 2007). The proposed Hyperspectral Infra-Red Imager (HyspIRI) would carry a visible-shortwave infrared (VSWIR) hyperspectral sensor with AVIRIS-like spectral range (0.38–2.5 μm) and resolution (10 nm), but data would be acquired at a spatial resolution of 60.0 m. Fire detection and temperature modeling algorithms that have been developed for higher spatial resolution AVIRIS data have not been tested at coarser spatial resolutions. Spectral mixing of fire emitted radiance may change modeled fire temperature and area as spatial resolution is altered.

By resampling AVIRIS images to coarser spatial resolutions and applying fire detection and temperature modeling algorithms, the impacts of spatial resolution on retrieved fire parameters can be simulated. This study has three main objectives: (1) assess whether simple averaging of adjacent pixels (aggregation) can be used as a substitute for a less flexible, but more realistic Gaussian resampling approach; (2) assess the performance of fire detection and temperature modeling algorithms applied to images resampled to coarser

* Corresponding author. Tel.: +1 801 585 1805; fax: +1 801 581 8219.
E-mail address: dennison@geog.utah.edu (P.E. Dennison).

spatial resolutions; and (3) find a maximum shortwave infrared (SWIR) emitted radiance for 60.0 m spatial resolution data. By addressing each of these objectives, the abilities of HypSPRIR VSWIR data for characterizing fire can be estimated.

2. Background

Hyperspectral sensors measure radiance reflected from or emitted by a surface. Cooler temperature objects (i.e., temperatures up to 500 K) emit most of their radiance in the thermal infrared (8–12 μm) and middle infrared (3–5 μm) regions of the electromagnetic spectrum. Hotter temperature objects (e.g., smoldering and flaming combustion above temperatures of 500 K) emit more of their radiance in the SWIR (1.4–2.5 μm). Planck's equation specifies emitted blackbody radiance at a specific wavelength and temperature. If radiance is known and blackbody emissivity is assumed, the radiative temperature of the object can be estimated by inverting Planck's equation.

Temperature modeling for wildfires is complicated by the fact that pixels can contain mixed radiance that includes multiple combusting and non-combusting areas. The effective temperature and subpixel area of a fire within a pixel can be modeled using a spectral mixing model, which models pixel radiance as a combination of endmember radiances multiplied by their fractional area. Endmembers are spectrally pure signatures of a given land cover type (or radiance emitted at a specific fire temperature, in the case of wildfires), gathered from either field-measured spectra, relatively pure pixels in the image, or modeled radiance that accounts for atmospheric effects through radiative transfer modeling (Eckmann et al., 2008). The general equation for spectral mixing is:

$$L_{\lambda} = \sum_{i=1}^N f_i L_{i\lambda} + \varepsilon_{\lambda} \quad (1)$$

where L_{λ} is the total mixed spectral radiance for the pixel, $L_{i\lambda}$ is the radiance of endmember i at wavelength λ , f_i is the fraction of endmember i , N is the number of endmembers, and ε_{λ} is the residual error. In the case of modeling fire in SWIR wavelengths, the fraction and radiance terms can represent reflected solar radiance or emitted radiance from a fire. The first spectral mixing model applied to temperature retrieval of wildfires was developed by Dozier (1981) for the Advanced Very High Resolution Radiometer (AVHRR). This method uses a two endmember model which employs two broadband AVHRR channels at 4 μm and 11 μm to spectrally discriminate between fire and nonfire (cool background) endmembers. The method uses the following equation:

$$L_{\lambda} = f_f \beta(\lambda, T_f) + f_b \beta(\lambda, T_b) \quad (2)$$

where f_f is the fire fractional area, f_b is the background fractional area, T_f is the fire temperature, T_b is the background temperature, and β is Planck's equation. Giglio and Kendall (2001) note that the method is based on the following assumptions: all objects and background emit as blackbodies, a hot object has a single, uniform temperature, atmospheric effects are minimal, and that nearby pixels may be used to estimate radiance for nonfire portions of a fire pixel.

2.1. Fire detection in hyperspectral data

Hyperspectral fire detection indices based on three spectral features have been proposed. Vodacek et al. (2002) and Amici et al. (2011) examined fire detection based on near infrared bands that capture potassium emission found in burning vegetation. Dennison (2006) introduced a carbon dioxide absorption index using a combination of three bands to indicate reduced carbon dioxide absorption

caused by the limited path length of emitted radiance. Dennison and Roberts (2009) used kappa matrices to compare all potential paired combinations of AVIRIS bands, and termed the most accurate pair the Hyperspectral Fire Detection Index (HFDI):

$$\text{HFDI} = \frac{(L_{2.43\mu\text{m}} - L_{2.06\mu\text{m}})}{(L_{2.43\mu\text{m}} + L_{2.06\mu\text{m}})} \quad (3)$$

HFDI is based on both trace gas absorption and differences in the spectral shapes of reflected solar radiance and fire emitted radiance caused by Planck's equation. The value increases as the emitted radiance contribution to total radiance increases. Dennison and Roberts (2009) evaluated the performance of HFDI against the potassium emission index (Vodacek et al., 2002) and the carbon dioxide index (Dennison, 2006) on AVIRIS scenes of the 2007 Zaca Fire and the 2008 Indians Fire in California. They found that HFDI outperformed the other indices, with less sensitivity to smoke than the potassium emission index and less background noise than the carbon dioxide index. However, simulations did show that HFDI has decreased sensitivity to fire at modeled temperatures below 750 K and above 1400 K.

2.2. Hyperspectral fire temperature modeling

Modeling of fire temperature using hyperspectral data has built upon the mixing model approach of Dozier (1981). Green (1996) used observable spectral differences between emitted radiance and reflected solar radiance to model fire temperature. Dennison et al. (2006) improved upon the Green (1996) methods by applying multiple endmember spectral mixture analysis (MESMA; Roberts et al., 1998) to modeling fire temperatures. This method uses a spectral library of endmembers, and establishes the best fit combination of endmembers for each image spectrum. Dennison et al. (2006) used MESMA to compare and select the best fit combination of a reflected solar radiance endmember (from a spectral library of selected image endmembers), an emitted radiance endmember (from a spectral library of modeled emitted radiance endmembers for temperatures ranging from 500 to 1500 K), and a shade (no measured radiance) endmember. While the method was computationally intensive and produced some errors due to smoke and sensor saturation in the SWIR, it effectively combined temperature modeling and fire fractional area estimation with background land cover classification. Dennison and Matheson (2011) improved upon the Dennison et al. (2006) fire temperature algorithm by using HFDI for fire detection, as well as separate spectral libraries of background endmembers for smoke, nonsmoke, and fire pixels. The algorithm was applied to both AVIRIS data and coarser spatial resolution data from the MODIS/ASTER Airborne Simulator (MASTER), but differences in modeled temperature due to spatial resolution were not examined.

2.3. Spatial rescaling

A primary limitation on the ability to characterize land cover or model temperature in remotely sensed imagery is the spatial resolution of the imagery itself. Coarser spatial resolutions can result in a loss of spatial and spectral information. Multiple studies have examined the impact of spatial resolution on mapping of vegetation. Bian (1997) showed that variability in the values of a Landsat TM reflectance/absorptance biomass index decreased with coarsening spatial resolution. Walsh et al. (1997) also demonstrated that biomass variation was scale dependent, noting a smoothing of NDVI values at coarser resolutions. Nelson et al. (2009) coarsened Landsat TM and ETM+ imagery to facilitate forest boundary detection, but found that different thresholds must be set depending on the spatial resolution to avoid under- and over-detection of a boundary. Rahman et al. (2003) used spatial upscaling (coarsening of spatial

resolution) to determine the best spatial resolution for studying properties of grassland and chaparral using AVIRIS data. Schaaf et al. (2011) combined spatial scaling and MESMA to map vegetation in the Wasatch Mountain Range, Utah, USA, across multiple spatial resolutions of resampled AVIRIS data.

Relatively few studies have examined multiscale approaches to temperature retrieval. Anderson et al. (2007) used data with differing spatial scales acquired from airborne and spaceborne sensors to produce a land-atmosphere transfer scheme to compare changes in land surface temperature at high temporal and spatial resolutions. Finer spatial resolution data from Landsat Enhanced Thematic Mapper + (ETM+) and the Advanced Thermal Emission and Reflection Radiometer (ASTER) data have been frequently used to assess fire detection or retrieval of fire properties from coarser spatial resolution MODIS or GOES data (Csiszar & Schroeder, 2008; Csiszar et al., 2006; Eckmann et al., 2008, 2009, 2010; Kushida, 2010; Morisette et al., 2005a, 2005b; Schroeder et al., 2008). To date, no studies have examined the impact of spatial scaling on hyperspectral fire detection and temperature retrieval. Spatial scaling analysis using hyperspectral data may provide valuable information for the development of wildfire applications for future coarser spatial resolution hyperspectral sensors like HypsIRI.

3. Methods

3.1. Image data

AVIRIS has 224 contiguous spectral bands, and each band has an approximate 10 nm bandwidth. The AVIRIS sensor has an instantaneous field of view (IFOV) of 1 mrad, which produces spatial resolutions ranging from approximately 4 m to 20 m, depending on the height of the platform above the Earth's surface. Each of the four AVIRIS scenes used in this research was acquired from one of two airborne platforms: an ER-2 used for high altitude missions, or a Twin Otter that flies at lower altitudes and acquires finer spatial resolution images. All AVIRIS data were delivered as radiometrically calibrated products, with geometric correction and geographic referencing provided by onboard global positioning system and inertial data (Boardman, 1999). For the geometric correction process, the output spatial resolution was specified to be equal to the calculated ground IFOV based on reported platform and terrain height. The four AVIRIS fire scenes are shown in Figs. 1 and 2.

The Simi Fire burned a total of 438 km² from its start on 25 October 2003 to 5 November 2003. The AVIRIS sensor onboard a Twin Otter platform collected data over the Simi Fire in the Santa Susana Mountains north of Los Angeles, California, USA on 27 October 2003 (Table 1). The resulting geometrically corrected AVIRIS scene had a spatial resolution of 5.0 m.

The Zaca Fire burned nearly 1000 km² in Santa Barbara County, California from 4 July 2007 to 2 September 2007, making it one of the largest and most expensive fires in California history (California Department of Forestry & Fire Protection, 2007). The AVIRIS sensor onboard a Twin Otter platform acquired data over an active portion of the fire on 12 August 2007 (Table 1). The resulting geometrically corrected AVIRIS scene had a spatial resolution of 4.7 m.

In June 2008, the Indians Fire burned approximately 300 km² of the Santa Lucia Mountains along the central coast of California. AVIRIS data were acquired from an ER-2 platform on 11 June 2008 (Table 1). The geometrically corrected AVIRIS scene for the Indians Fire had a spatial resolution of 19.5 m.

The 2009 Station Fire burned 650 km² from 16 August to 16 October 2009 in the San Gabriel Mountains in Los Angeles County, California. On 31 August 2009, data were collected for the fire area by AVIRIS onboard an ER-2 platform. The majority of the active fire was covered in four flight lines, with a varying spatial resolution ranging between approximately 10 and 14 m. The imagery from "run 10" was selected for this study because it contained a large portion of the actively

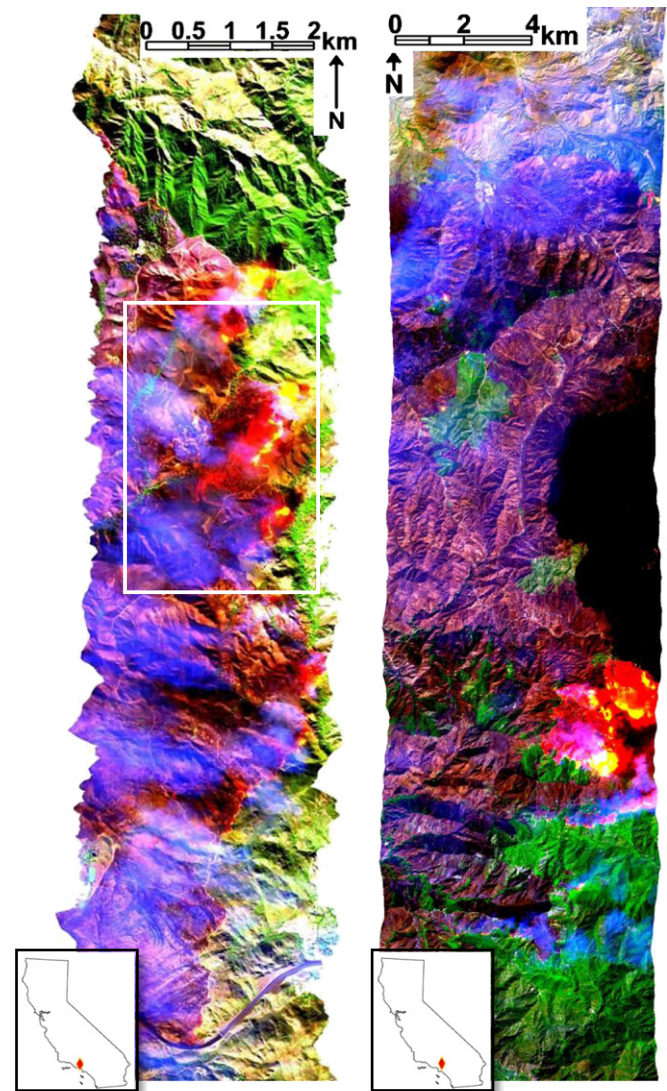


Fig. 1. AVIRIS scenes containing the 2003 Simi Fire (left) and 2009 Station Fire (right). The online figure shows false color composites based on bands centered at approximately 1.7 μm (red), 1.1 μm (green), and 0.66 μm (blue). The Simi Fire image includes a white box that denotes a spatial subset used for Figs. 4–5 and 8. (For interpretation of the references to color in this figure legend, the reader is referred to the web version of this article.)

burning fire and was minimally covered by a large pyrocumulus cloud present over other portions of the active fire. The geometrically corrected AVIRIS scene had a spatial resolution of 13.2 m.

The center wavelengths and full-width half-maxima (FWHM) of AVIRIS bands change over time as the sensor is upgraded, so bands were subset independently for each AVIRIS scene. Spectra from each scene were visually examined to determine bands containing water vapor absorption or scattering from smoke. Bands with wavelengths shorter than 1.2 μm contained degradation from smoke scattering (Dennison et al., 2006), and bands centered near atmospheric water vapor absorption features were rejected. A total of 54 NIR and SWIR bands were used for modeling the Zaca, Indians and Station Fire scenes, and 55 bands were used for modeling the Simi Fire scene.

Gaussian resampling of 5.0 m AVIRIS data using a 60.0 m FWHM should closely approximate the expected point spread function of the HypsIRI VSWIR sensor (Robert Green, JPL, personal communication). However, Gaussian resampling can obscure spatial scaling effects, since the resampled spectrum is unevenly drawn from a larger

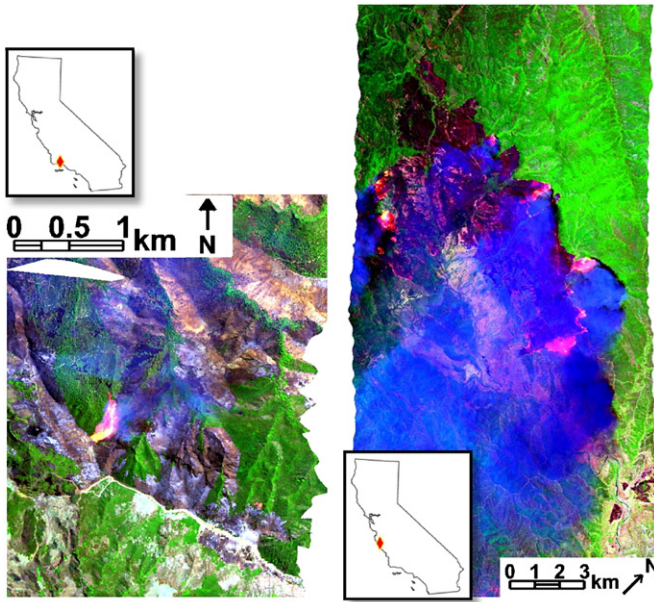


Fig. 2. AVIRIS scenes containing the 2007 Zaca Fire (left) and 2008 Indians Fire (right). The online figure shows false color composites based on bands centered at approximately 1.7 μm (red), 1.1 μm (green), and 0.66 μm (blue). (For interpretation of the references to color in this figure legend, the reader is referred to the web version of this article.)

area than the target spatial resolution. Pixel aggregation, which averages radiance from a square of pixels to create one new coarser resolution pixel, facilitates direct comparison between multiple spatial resolutions and is simpler to implement. The Simi Fire image, which had the best combination of high spatial resolution (5.0 m) and widest range of fire behavior, was used to compare the two resampling methods. Gaussian resampling used a 24 by 24 pixel kernel with a FWHM of 12 pixels (60.0 m). Aggregation resampling used averaged blocks of 12 by 12 pixels to create each 60.0 m pixel. For both types of resampling, a saturation mask was used during the resampling to prevent saturated spectra from being averaged with nonsaturated spectra of other nearby pixels. The saturation mask assigned null values to bands with saturation, thus keeping the resampled pixels from being spectrally distorted. However, saturation masking may have reduced area modeled at high fire temperatures, since pixels containing hot fires are more likely to occur adjacent to saturated pixels.

Radiance values compared across multiple wavelengths demonstrated that the Gaussian and aggregation resampling methods produced similar radiance values (Fig. 3). Saturation masking resulted in the exclusion of more Gaussian resampled pixels than aggregation resampled pixels, since the Gaussian resampling drew from a larger area (24 by 24 pixels vs. 12 by 12 pixels). When saturated bands were excluded, the radiance produced by the two resampling methods was very strongly correlated with a slope close to one (Fig. 3). Based on the similarity in resampled radiance, aggregation was used for further analysis of all four AVIRIS scenes.

The four original resolution AVIRIS images were resampled by doubling the resampling factor (Table 1). To achieve the final resolution closest to 60.0 m, the original resolution images for each fire were resampled by varying factors once doubling the resolution would far exceed the target 60.0 m. For the Simi Fire data, the 5.0 m resolution data were resampled by a factor of 12, producing an image with 60.0 m spatial resolution. The Zaca Fire data were resampled by a factor of 13 from a resolution of 4.7 m to 61.1 m. The 19.5 m resolution Indians Fire data were resampled by a factor of three, producing an image with a resolution of 58.5 m. The 13.2 m

Station Fire data were resampled by a factor of five, producing a 66.0 m image. The same saturation masking technique described above was used for all resampled images.

3.2. Modeling

Fire detection and temperature modeling closely followed the methods described in Dennison and Matheson (2011). HFDI was used to flag pixels likely to contain fire (Dennison & Roberts, 2009). The index produces values within the range of -1 to 1 , with high positive values indicating a greater likelihood of fire in a pixel. The threshold for fire detection is dependent on solar zenith angle and atmospheric water vapor concentration (Dennison & Roberts, 2009), so an appropriate threshold must be selected by the user. HFDI was calculated for each AVIRIS image and at each spatial resolution using the bands with center wavelengths closest to 2.06 and 2.43 μm . The following threshold values were empirically selected for the finest resolution fire scenes: 0.00 (Simi), -0.15 (Zaca), 0.00 (Indians), and -0.10 (Station). The threshold for each scene was applied to all spatial resolutions as a controlled variable to uniformly assess the effects of changing spatial resolution on fire detection and temperature modeling. Total area of fire detection was directly compared between all spatial resolutions using the Lee–Sallee shape index (Lee & Sallee, 1970). This index is generated by dividing the intersecting area of fire detection in two images by the union of the area of fire detection in both images. Values range from 0 to 1, where 0 indicates no agreement and 1 indicates total agreement.

Pixels with HFDI values below the fire detection threshold were modeled using a two-endmember linear spectral mixing model to map background land cover. This model has the form:

$$L_{\lambda} = f_b L_{\lambda b} + f_s L_{\lambda s} + \epsilon_{\lambda} \tag{4}$$

where $L_{\lambda b}$ is the radiance of the background endmember at that wavelength, $L_{\lambda s}$ is the radiance of the shade endmember accounting for atmospheric scattering, and f_b and f_s are the fractions of each endmember (which sum to 1). The sum of the residual errors for all wavelengths was used to calculate root mean square error (RMSE). All unsaturated pixels with HFDI values exceeding the indicated thresholds were modeled with a three-endmember linear spectral mixing model to retrieve fire temperature:

$$L_{\lambda \text{ sensor}} = f_{ef} L_{\lambda ef} + f_b L_{\lambda b} + f_s L_{\lambda s} + \epsilon_{\lambda} \tag{5}$$

Table 1

Characteristics of the four original AVIRIS images and their coarsened spatial resolutions. The asterisk indicates that two resampled images were generated at this spatial resolution to compare aggregation and Gaussian resampling methods.

Fire	Simi	Zaca	Indians	Station
Platform	Twin Otter	Twin Otter	ER-2	ER-2
Scene date	27-Oct-2003	12-Aug-2007	11-Jun-2008	31-Aug-2009
Latitude	34.33°	34.62°	36.07°	34.28°
Longitude	-118.65°	-119.78°	-121.38°	-118.11°
Mean scene time (UTC)	21:05	21:52	20:31	18:34
Solar zenith angle	52.5°	31.3°	14.07°	31.3°
Mean ground elev. (m)	650	710	776	1078
Mean sensor elev. (km)	5.6	5.6	20.1	14.3
Atmospheric water vapor concentration (atm-cm)	864	898	493	1069
Original resolution (m)	5.0	4.7	19.5	13.2
Resampled resolutions (m)	10.0, 20.0, 40.0, 60.0*	9.4, 18.8, 37.6, 61.1	39.0, 58.5	26.4, 52.8, 66.0

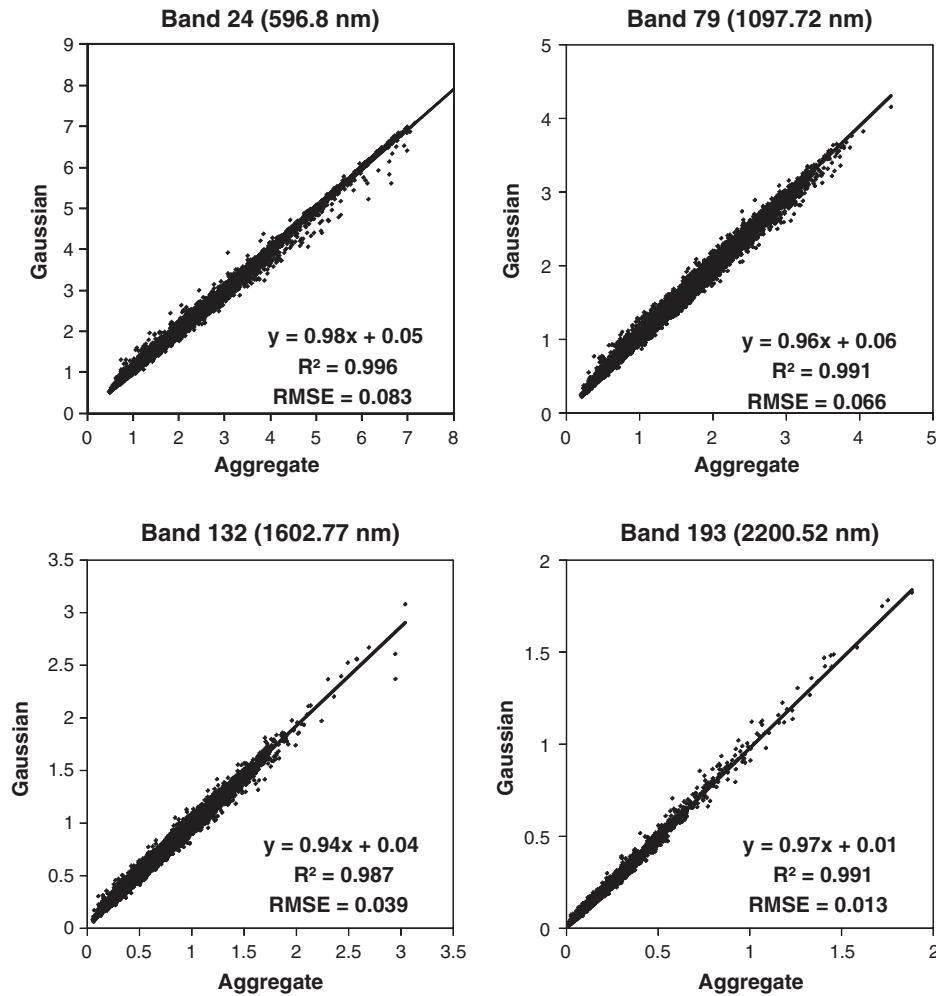


Fig. 3. Scatterplots comparing radiance values (in $\mu\text{W cm}^{-2} \text{sr}^{-1} \text{nm}^{-1}$) at four wavelengths for 60.0 m pixels resampled from the Simi Fire scene. X-axis values were calculated using aggregation resampling, and y-axis values were calculated using Gaussian resampling.

where $L_{\lambda EF}$ is the radiance of the emitted radiance endmember and f_{EF} is its associated fraction.

The emitted radiance and shade endmembers were modeled using the radiative transfer model MODTRAN 5.2 (Berk et al., 1989), while the background endmembers were selected from each of the four finest spatial resolution AVIRIS images. The same sets of endmembers were applied to all spatial resolutions of each fire scene to isolate the effects of changing spatial resolution on fire temperature modeling.

To create the emitted radiance spectral libraries, a total of 101 blackbody endmembers were modeled for each fire scene for temperatures ranging from 500 to 1500 K at 10 K intervals. Temperatures lower than 500 K were not used because Dennison et al. (2006) and Dennison and Roberts (2009) observed that the limited radiance that did exist in the SWIR for these cooler fire temperatures was unreliable for fire detection and temperature modeling. A mid-latitude summer atmospheric model was used for all MODTRAN simulations, with image visibility for all images set to 23 km. This was an overestimate of the visibility within the smoky portions of the scenes, but lowering visibility did not substantially change modeled radiance at wavelengths used for modeling. ACORN (ImSpec LLC) reflectance retrieval software was used to produce an average atmospheric water vapor concentration in areas near the fires within each scene (Table 1). These water vapor concentrations were used as inputs in MODTRAN to create the emitted radiance spectra. Output MODTRAN radiance spectra were convolved to AVIRIS bands using band centers and FWHM before being added to an endmember library

for each fire. Like the emitted radiance endmembers, the shade endmembers were modeled for each fire scene using MODTRAN. This endmember contains only modeled atmospheric scattering, without emitted or reflected radiance (Eckmann et al., 2008). Each of the generated shade endmembers was convolved to AVIRIS band centers and FWHM.

Background radiance endmembers were used to account for reflected solar radiance. Following the methodology described in Dennison and Matheson (2011), separate libraries were generated for smoky and nonsmoky portions of each scene to avoid misclassification due to scattering by smoke. A smoke mask was generated for the original spatial resolution of each fire scene using a maximum likelihood classification. The masks were spatially resampled to the coarser resolutions by averaging and rounding the averaged mask values to either zero or one for smoke or non-smoke classification. The background endmembers were selected from image spectra representing six land cover classes from each original, finest spatial resolution image. All of the scenes were acquired over mountainous areas in either central or southern California, areas which share some broad vegetation characteristics. For example, dense and sparse stands of chaparral shrubland are common in the region, taller stands of oak forest are located in riparian areas and north-facing slopes, and grasses are found in disturbed areas (Dennison et al., 2006). Other non-vegetated land cover types used for background modeling included soil and rock (grouped into the same class) and ash. In the Indians Fire scene, a second class of ash was created to prevent over-modeling of

grass in the smoke portion of the image (Dennison & Matheson, 2011).

An iterative endmember selection algorithm (Schaaf et al., 2011) was used to find the reduced set of background endmembers that was still able to accurately classify the selected background spectra. Kappa coefficient (Cohen, 1960) was used to assess the accuracy of background spectrum classification. The iterative endmember selection algorithm was run until the kappa coefficient reached a minimum of 0.895, or until the improvement in kappa gained by adding additional endmembers reached a threshold of 0.0025. The final selected endmembers were then assigned to the three categories: 1) smoke, 2) nonsmoke, and 3) fire. The fire category endmembers used for modeling fire-flagged pixels included soil/rock and ash endmembers from smoky portions of the image, which were also included in the library to be used to model smoke-flagged pixels.

Each radiance image, paired with a smoke mask and an HFDI mask, was modeled using MESMA. If a pixel had an HFDI value higher than the HFDI threshold, it was modeled with three endmembers: an emitted radiance endmember, a shade endmember, and a background endmember from the fire library. If a pixel had an HFDI value lower than the threshold, it was modeled with two endmembers: a shade

endmember, and a background endmember from the smoke library if the smoke mask flagged that pixel, or a background endmember from the nonsmoke library if no smoke was present.

Singular-value decomposition was used to fit all possible combinations of endmembers from the appropriate libraries in order to solve for the endmember fractions that best modeled each pixel spectrum. Saturated bands were removed from modeling using the saturation radiance value for each band, and pixels were required to have two or more nonsaturated bands for modeling. Endmember fractions were constrained to between 0 and 1. The model that produced the lowest RMSE was assigned to each pixel.

Modeled temperature and fire fractional areas were compared between all spatial resolutions of each fire scene. Modeled temperatures were summed by fire fractional area to calculate the total area modeled at each temperature at each spatial resolution. The Kolmogorov–Smirnov (K–S) statistic, a nonparametric test (Massey, 1951), was used to compare the histograms of area modeled at each temperature across the range of spatial resolutions. A *p*-value threshold of 0.05 was used, with values lower than the threshold indicating a failure to reject a null hypothesis of no difference between two temperature-area distributions.

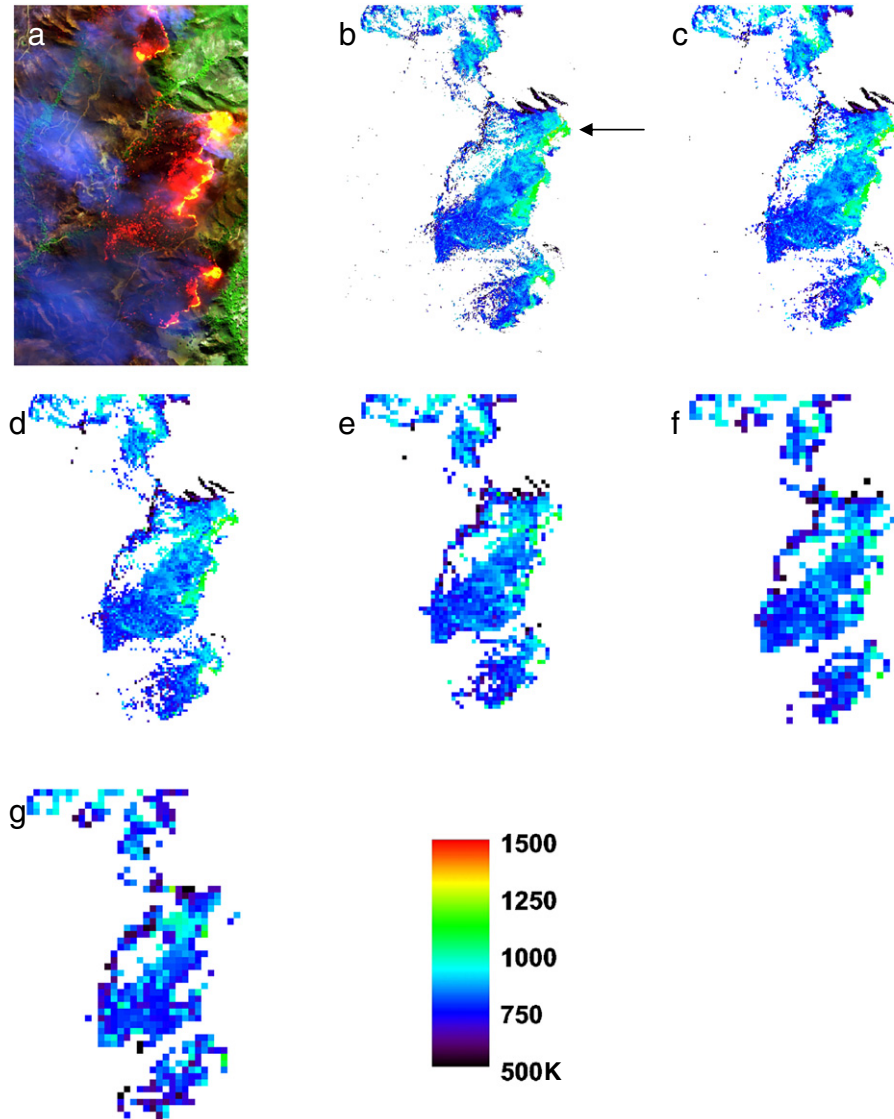


Fig. 4. A subset of the Simi Fire radiance image at 5.0 m (a) and modeled temperatures at spatial resolutions of 5.0 m (b), 10.0 m (c), 20.0 m (d), 40.0 m (e), 60.0 m aggregation resampled (f), and 60.0 m Gaussian resampled (g). The arrow indicates a hotspot that partially disappears due to saturation masking.

4. Results

Modeled temperature (Fig. 4) and fire fractional area (Fig. 5) are shown for the Simi Fire, including the 60.0 m resolution images comparing the two resampling methods (Figs. 4f–g and 5f–g). In these figures, the fire is moving from left to right, with the higher temperature fire front extending from top to bottom on the right side of the image. Fig. 4 illustrates similar trends in the spatial distribution of temperatures across all spatial resolutions. The majority of the fire was modeled with temperatures between 700 and 1000 K, with the hottest temperatures modeled for pixels along the fire front. Higher temperatures were modeled along the fire front at finer spatial resolutions (green hues in Fig. 4), but as the resolution coarsened the modeled temperature in these same areas decreased. Saturation masking also reduced the area modeled with high temperatures as spatial resolution coarsened. For example, there is a large hotspot along the fire front (indicated by the arrow in Fig. 4b) where the modeled area decreases while the masked saturated area increases due to aggregation. Small areas of elevated temperature were mapped ahead of the fire front due to scattering of emitted radiance coming from the hot-burning fire front (Dennison & Matheson, 2011).

The 60.0 m Gaussian resampled image (Fig. 4g) contains several additional pixels modeled with fire temperature compared to the 60.0 m pixel aggregation resampled image (Fig. 4f). Most of these additional pixels in the Gaussian resampled image were modeled with low fire temperatures. Notably, the Gaussian resampled image had fewer modeled pixels along the fire front due to the saturation masking procedure. For a given band, if any pixel with the 24 by 24 kernel area was saturated, then that band was assigned a null value for the resampled pixel. This resulted in a larger number of pixels where all useable bands were saturated – the Gaussian resampled image had 169 pixels masked as saturated, more than double the aggregation resampled image's 64 pixels.

Similarly, spatial distributions of fire fractional area appeared to remain largely consistent across multiple spatial resolutions (Fig. 5). In general, the highest fire fractional areas were modeled along the fire front. Again, larger saturated areas were left unmodeled at coarser resolutions. As spatial resolution coarsened to 60.0 m, fire fractional area increased behind the fire front. The additional pixels modeled in the Gaussian resampled image possessed low fire fractions (Fig. 5g).

Images for the other three fires (not shown) displayed similar patterns as spatial resolution was coarsened. The highest temperatures

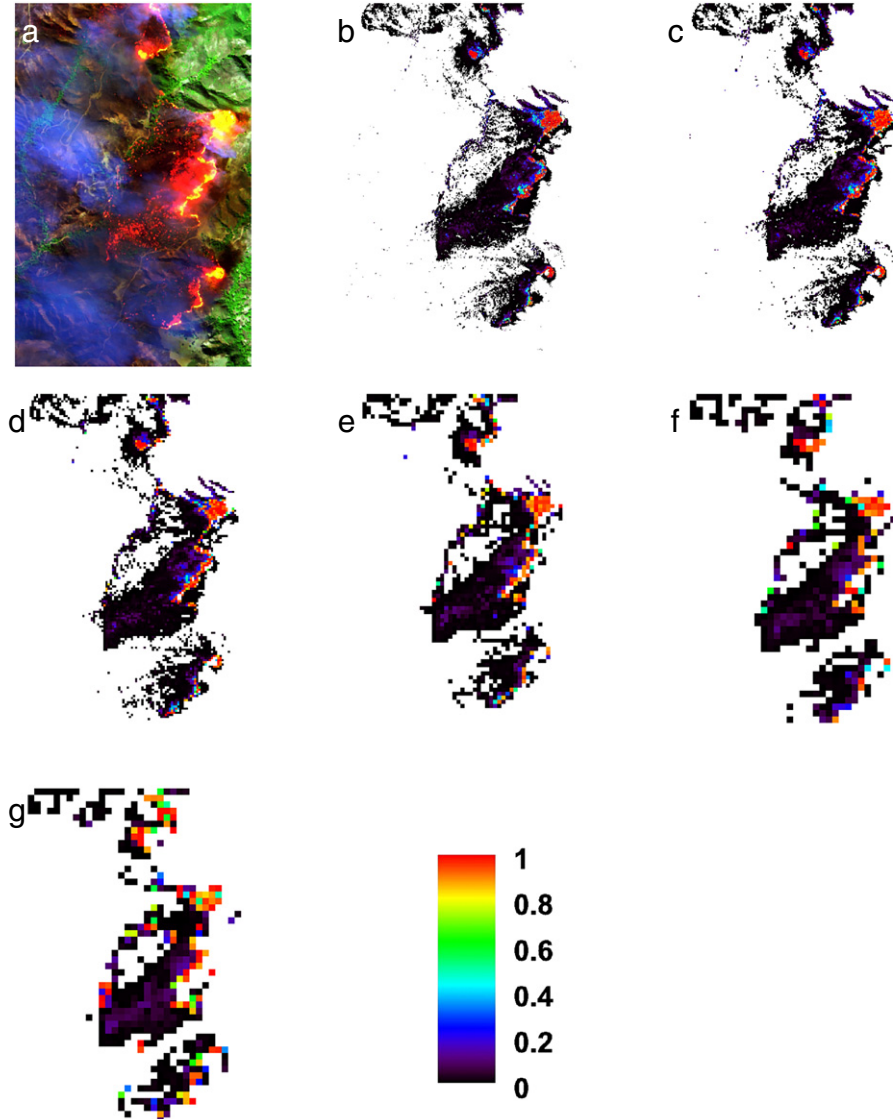


Fig. 5. A subset of the Simi Fire radiance image at 5.0 m (a) and modeled fire fractional area at spatial resolutions of 5.0 m (b), 10.0 m (c), 20.0 m (d), 40.0 m (e), 60.0 m aggregation resampled (f), and 60.0 m Gaussian resampled (g).

and fire fractions were found along fire fronts, although fire front modeled temperature decreased with coarsening spatial resolution. With coarsening spatial resolution, fire fractional area increased in lower temperature areas behind the fire fronts. These observations agree with the broad trends captured by the mean modeled temperature and fractional area for each fire scene (Table 2). As spatial resolution coarsened, mean temperature decreased and fire fractional area increased for all four fires.

By multiplying the dimensions of each pixel by its fire fractional area, total area modeled was calculated and compared with HFDI-flagged area for each fire scene (Table 3). HFDI flagged far more area for fire, since area was assessed based on entire pixels, not accounting for fire fractional area. In all cases, coarsening spatial resolution resulted in increased area. The trend for the Zaca, Indians and Station Fires was that the coarsest spatial resolution modeled approximately 1.5 times the original resolution's total modeled fire area. However, the Simi Fire aggregation resampled 60.0 m data modeled nearly three times the total fire area of the 5.0 m data. Both HFDI and the modeled area were much higher for Gaussian resampling compared to aggregation resampling, likely due to the introduction of low amounts of emitted radiance to a larger number of pixels through the larger Gaussian resampling kernel.

Spatial agreement in HFDI-flagged area between different spatial resolutions, as assessed by the Lee–Sallee index, was consistently highest for the comparison of the finest resolution and the first resampled resolution (Table 4). Agreement was higher for closer spatial resolutions (e.g., 10.0 m and 20.0 m), and decreased for more widely separated spatial resolutions (e.g., 10.0 m and 60.0 m). Table 4 also shows a pattern of decreasing Lee–Sallee values between sequential resolutions as spatial resolution coarsened (e.g., values along the diagonal for each fire). Overall agreement was best between the 4.7 m and 9.4 m resolutions of the Zaca Fire, with a Lee–Sallee value of 0.887. The Station Fire produced the poorest agreement, with a Lee–Sallee value of 0.567 between the 13.2 m and 66.0 m resolutions. The aggregation and Gaussian resampled Simi Fire images produced a Lee–Sallee value of 0.682, indicating moderate agreement.

The histograms of total area modeled at each temperature were plotted on a logarithmic scale to highlight differences across a wide

Table 2
Summary of mean modeled temperature and fractional area for all spatial resolutions of each fire scene.

Fire	Resolution	Mean modeled temp (K)	Mean fraction
Simi	5.0 m	812	0.073
	10.0 m	809	0.079
	20.0 m	803	0.099
	40.0 m	790	0.134
	Aggregation 60.0 m	780	0.168
	Gaussian 60.0 m	758	0.251
Zaca	4.7 m	696	0.239
	9.4 m	689	0.273
	18.8 m	676	0.327
	37.6 m	669	0.382
	61.1 m	663	0.408
Indians	19.5 m	779	0.169
	39.0 m	773	0.192
	58.5 m	765	0.219
Station	13.2 m	845	0.131
	26.4 m	834	0.145
	52.8 m	809	0.176
	66.0 m	804	0.187

Table 3
Total HFDI-flagged area and modeled fire area for all spatial resolutions of each fire scene.

Resolution	Total HFDI-flagged area (km ²)	Total modeled fire area (km ²)
Simi		
5.0 m	3.379	0.204
10.0 m	3.500	0.230
20.0 m	3.776	0.306
40.0 m	4.267	0.444
60.0 m aggregation	4.849	0.572
60.0 m Gaussian	6.538	0.867
Zaca		
4.7 m	0.170	0.033
9.4 m	0.169	0.038
18.8 m	0.173	0.047
37.6 m	0.181	0.053
61.1 m	0.194	0.055
Indians		
19.5 m	9.719	1.360
39.0 m	10.182	1.641
58.5 m	10.606	1.957
Station		
13.2 m	20.066	1.669
26.4 m	20.298	1.865
52.8 m	20.555	2.233
66.0 m	20.534	2.474

range of modeled area (Fig. 6). All histograms exhibited the broad trend of decreasing area with increasing fire temperature, regardless of spatial resolution. Area modeled between 500 K and approximately 850 K increased with coarsening resolution for the Simi Fire (Fig. 6a). This trend reverses from 850 K to approximately 1150 K, with finer spatial resolutions exhibiting higher modeled area. Only the three finest resolutions had modeled area for temperatures above 1400 K. The temperature with the largest modeled area decreased with coarsening spatial resolution: 860 K for 5.0 m, 840 K for 10.0 m, 800 K for both 20.0 m, 740 for 40.0 m, and 700 K for 60.0 m.

By plotting the total area modeled at each temperature for the two 60.0 m resampled images of the Simi Fire (Fig. 7), differences between the two resampling methods became clearer. Gaussian resampling resulted in more modeled area for temperatures between 500 and 700 K. Both resampling methods produced the largest modeled area in this range; 670 K for Gaussian resampling and 700 K for aggregate resampling. The Gaussian resampled image had at maximum temperature of 1230 K, while the aggregation resampled image had an outlying maximum temperature of 1350 K.

Table 4
Lee–Sallee shape index results comparing HFDI-flagged area for all spatial resolutions of the Simi, Zaca, Indians, and Station Fires.

Fire	Resolution 1	Resolution 2	Resolution 3	Resolution 4	Resolution 5
Simi	10.0 m	20.0 m	40.0 m	60.0 m	
	5.0 m	0.813	0.716	0.621	0.666
	10.0 m		0.775	0.662	0.585
	20.0 m			0.731	0.641
	40.0 m				0.676
Zaca	9.4 m	18.8 m	37.6 m	61.1 m	
	4.7 m	0.887	0.816	0.726	0.610
	9.4 m		0.857	0.746	0.622
	18.8 m			0.768	0.635
	37.6 m				0.678
Indians	39.0 m	58.5 m			
	19.5 m	0.790	0.726		
	39.0 m		0.771		
Station	26.4 m	52.8 m	66.0 m		
	13.2 m	0.818	0.732	0.567	
	26.4 m		0.788	0.746	
	52.8 m			0.789	

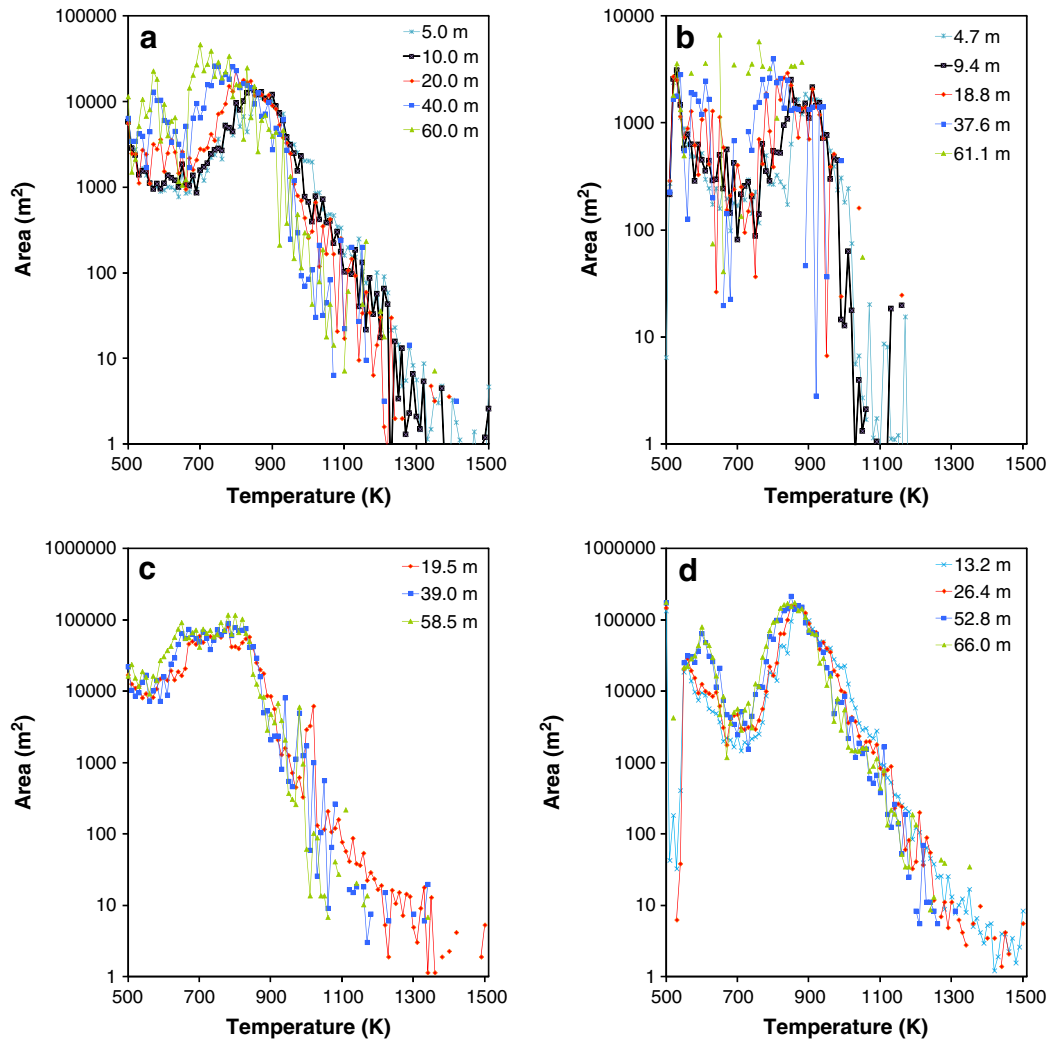


Fig. 6. Histograms showing total area modeled at each temperature for all spatial resolutions of the Simi Fire (a), Zaca Fire (b), Indians Fire (c), and Station Fire (d). Temperatures for which no area was modeled are not shown, which produces “missing lines” between some individual points.

Histograms for the five resolutions of the Zaca Fire scene (Fig. 6b) demonstrated similar patterns to those of the Simi Fire, albeit on a smaller scale, since the fire captured in the scene was much smaller. For the range of temperatures from 500 K to approximately 900 K, greater area was typically modeled for coarser resolutions. Modeled area dropped considerably for temperatures beyond 900 K for all spatial resolutions, with the two finest resolutions dominating the area modeled above 1000 K. There was a very small area modeled at 1500 K for the 4.7 m data (0.11 m^2). The highest temperatures modeled for the coarser resolutions were 1050 K for the 61.1 m data, and only 990 K for the 52.8 m data.

For the Indians Fire scene (Fig. 6c), the peak area modeled for all three resolutions was at 780 K. Coarser spatial resolutions had higher modeled area below 820 K. At higher temperatures, trends between spatial resolution and modeled area are less evident. The highest modeled temperatures were 1500 K for 19.5 m, and 1340 K for both 39.9 m and 58.5 m. Total area modeled at each temperature produced similar histograms for the Station Fire (Fig. 6d). With the exception of the temperature range 510–680 K, area modeled for temperatures below 1050 K remained relatively consistent across all spatial resolutions. The largest area for all resolutions – except for 66.0 m at 500 K – was modeled in the same mid-temperature range: at 870 K for 13.2 m, 860 K for 26.4 m, and 850 K for 52.8 m data. All spatial resolutions produced reduced modeled area for 510–540 K, while the 52.8 m data modeled no

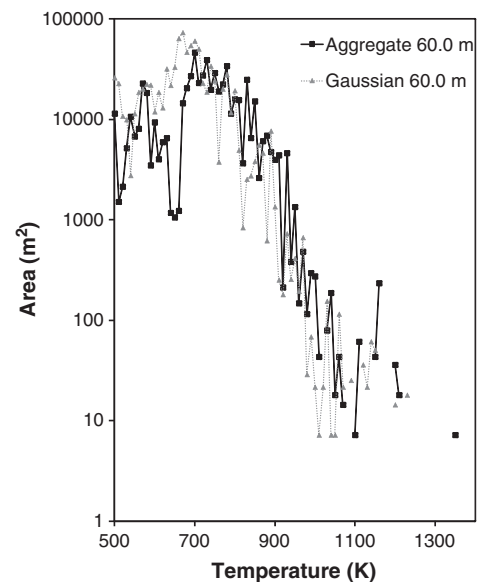


Fig. 7. Histograms showing total area modeled at each temperature for the Simi Fire comparing two resampling methods at 60.0 m spatial resolution. Temperatures for which no area was modeled are not shown, which produces “missing lines” between some individual points.

Table 5

Kolmogorov–Smirnov statistics for comparisons of area modeled at each temperature for all spatial resolutions of the Simi, Indians, Zaca, and Station Fires. Shaded values have corresponding statistically significant *p*-values, indicating that the distributions are significantly different.

Simi				
	5.0 m	10.0 m	20.0 m	40.0 m
10.0 m	0.09			
20.0 m	0.20	0.15		
40.0 m	0.34	0.29	0.16	
60.0 m	0.37	0.32	0.17	0.08

Indians		
	19.5 m	39.0 m
39.0 m	0.23	
58.5 m	0.29	0.07

Zaca				
	4.7 m	9.4 m	18.8 m	37.6 m
9.4 m	0.17			
18.8 m	0.28	0.11		
37.6 m	0.38	0.21	0.12	
61.1 m	0.56	0.40	0.29	0.19

Station			
	13.2 m	26.4 m	52.8 m
26.4 m	0.12		
52.8 m	0.27	0.16	
66.0 m	0.27	0.16	0.06

area within this temperature range. For hotter temperatures, more area was generally modeled for the finer spatial resolutions, a trend similar to the Indians and Simi Fires.

The results from the Kolmogorov–Smirnov nonparametric tests between the temperature-area distributions at each spatial resolution

(Figs. 6 and 7) are summarized in Table 5. For all of the fires, the distributions from the finest resolution data and from the coarsest resolution data were statistically different. In general, the images display a trend where each resolution's distribution could not be considered statistically different from that of the next finest or coarsest resolution. The Kolmogorov–Smirnov test comparing the two resampling methods produced a *D*-statistic of 0.099 and a *p*-value of 0.683, indicating moderate correlation between the histogram distributions.

Mean RMSE values were assessed for pixels modeled at selected temperatures across all spatial resolutions of each fire scene (Table 6). Reference temperatures were selected based on a sufficient number of pixels modeled across all spatial resolutions, with target temperatures of 500, 700, 900, and 1100 K. The Zaca Fire did not have a sufficient number of pixels modeled at any temperature near 1100 K, so only three temperatures were examined for the Zaca Fire. Where the coarsening factor was doubled from the previous resolution, the number of pixels modeled at each temperature decreased approximately by a factor of four as spatial resolution coarsened. Higher modeled temperatures produced higher RMSE values due to increased radiance, but mean RMSE values tended to decrease as spatial resolution coarsened. Examination of residual spectra showed that residuals were largest near atmospheric water vapor absorption features, similar to trends observed by Dennison and Matheson (2011).

Table 6

Mean RMSE values (in $\mu\text{W cm}^{-2} \text{sr}^{-1} \text{nm}^{-1}$) for pixels modeled with specific temperatures at all resolutions of each fire scene.

Spatial resolution	Simi							
	520 K		710 K		910 K		1100 K	
	Pixels	Mean RMSE						
5.0 m	787	0.0397	1767	0.0270	2721	0.1269	262	0.1796
10.0 m	191	0.0360	503	0.0237	733	0.1151	64	0.1328
20.0 m	49	0.0352	143	0.0194	174	0.0890	13	0.0897
40.0 m	11	0.0248	45	0.0169	40	0.0471	6	0.0471
60.0 m	5	0.0190	9	0.0117	20	0.0439	1	0.0259

Spatial resolution	Simi 60 m comparison							
	530 K		700 K		920 K		1150 K	
	Pixels	Mean RMSE	Pixels	Mean RMSE	Pixels	Mean RMSE	Pixels	Mean RMSE
60.0 m aggregation	9	0.0476	34	0.0124	8	0.0253	2	0.0821
60.0 m Gaussian	8	0.0274	41	0.0101	13	0.0152	1	0.0011

Spatial resolution	Zaca					
	520 K		730 K		860 K	
	Pixels	Mean RMSE	Pixels	Mean RMSE	Pixels	Mean RMSE
4.7 m	783	0.1175	85	0.0539	144	0.1521
9.4 m	193	0.1201	21	0.0418	28	0.1589
18.8 m	53	0.1157	4	0.0199	5	0.1625
37.6 m	12	0.1005	1	0.0103	1	0.1728
61.1 m	4	0.1182	1	0.0123	1	0.1732

Spatial resolution	Indians							
	530 K		720 K		960 K		1140 K	
	Pixels	Mean RMSE	Pixels	Mean RMSE	Pixels	Mean RMSE	Pixels	Mean RMSE
19.5 m	121	0.0721	727	0.0691	306	0.0481	7	0.3065
39.0 m	25	0.0611	176	0.0596	74	0.0367	1	0.2253
58.5 m	15	0.0951	87	0.0475	28	0.0340	1	0.1550

Spatial resolution	Station							
	550 K		720 K		960 K		1140 K	
	Pixels	Mean RMSE	Pixels	Mean RMSE	Pixels	Mean RMSE	Pixels	Mean RMSE
13.2 m	2652	0.1433	232	0.0471	2171	0.1177	727	0.0685
26.4 m	742	0.1405	58	0.0342	524	0.1173	170	0.0632
52.8 m	212	0.1404	10	0.0262	121	0.0262	28	0.0557
66.0 m	129	0.1434	10	0.0278	92	0.0863	19	0.0557

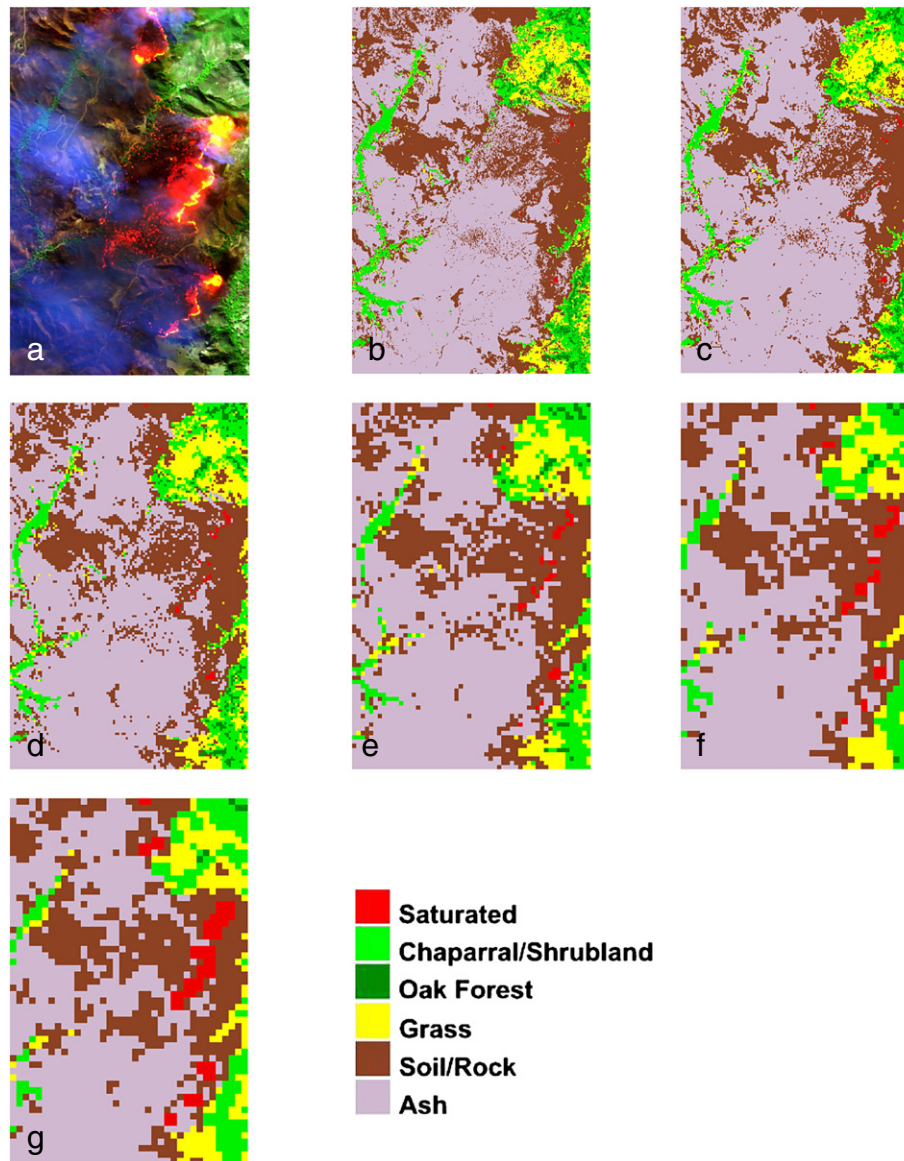


Fig. 8. A subset of the Simi Fire radiance image at 5.0 m (a) and background endmembers mapped at spatial resolutions of 5.0 m (b), 10.0 m (c), 20.0 m (d), 40.0 m (e), 60.0 m pixel aggregation resampled (f), and 60.0 m Gaussian resampled (g).

Background endmembers were modeled similarly across all spatial resolutions of all four fire scenes. An example is shown for the subset of the Simi Fire, including the 60.0 m images comparing the two resampling methods (Fig. 8). Qualitatively, classifications across all spatial resolutions match up very well with land cover as it appears in the radiance images, although spatial detail was lost with coarsening spatial resolution. The saturated area (in red) grew larger as spatial resolution coarsened. More pixels were saturated in the Gaussian resampled image than in the aggregation resampled image. Minor differences in the background classification occurred because of the difference in resampling methods. These differences consisted mostly of conflicts between soil/rock and ash, grass and soil/rock, and between the three vegetation classes. Due to the lack of *in situ* data for the areas within each AVIRIS scene, classification accuracies were not assessed for land cover types surrounding the fires.

5. Discussion

Coarsening spatial resolution did have an effect on modeled fire temperature and area, although the broad distributions of temperature and total fractional area remained similar. Coarser resolutions

produced larger areas of low fire temperature with lower modeling error. During spatial resampling, the radiance spectra of many smaller pixels (e.g., 4, 16, 64, and 256 for Simi, or 4, 16, 64 and 169 for Zaca) were averaged into those of a single larger pixel. Smaller pixels with higher radiance values resulting from hotter fire temperatures were averaged with more numerous lower radiance values from cooler fires and non-fire background reflected radiance, resulting in decreased area modeled at high temperatures and increased area modeled at low temperatures.

One of the limitations of temperature modeling is the assumption of single temperature blackbody emission, even though fire is spatially and temporally dynamic and highly variable across the smallest of distances. The emitted radiance measured within a single pixel can come from multiple combusting fuel elements, even at very high spatial resolutions. Furthermore, spectral radiance increases nonlinearly with temperature, so modeled temperatures within a pixel will be much more strongly impacted by hotter than by cooler objects. Thus, modeled temperature is an effective temperature based on the shape of emitted radiance and should not be directly equated with the kinetic temperature of the fire. Decreases in RMSE with coarsening spatial resolution indicate that fire emission may more closely

resemble blackbody emission when radiance is averaged over larger areas. Collection of *in situ* data in concert with high resolution hyperspectral data could improve understanding of both the spatial distribution of emitted radiance and correlations between modeled temperature and temperature measured on the ground.

Saturation of the AVIRIS instrument had a major impact on modeling, especially at coarser spatial resolutions where large numbers of SWIR bands were frequently masked. While the saturation mask ensured that saturated bands in high radiance pixels were excluded from modeling, it also resulted in a loss of valid information when the same bands were discarded from adjacent nonsaturated pixels included in resampling. AVIRIS saturation thresholds in the SWIR ranged from approximately $5 \mu\text{W cm}^{-2} \text{sr}^{-1} \text{nm}^{-1}$ in the Simi Fire scene to approximately $8 \mu\text{W cm}^{-2} \text{sr}^{-1} \text{nm}^{-1}$ in the Station Fire scene. To find a potential maximum SWIR radiance value at the spatial resolution of HypsIRI, modeled temperature and fractional area from the Simi Fire 60.0 m Gaussian-resampled data were used to calculate synthetic blackbody emission spectra for saturated bands. The pixel with the highest theoretical emitted radiance possessed a temperature of 890 K and a fire fractional area of 0.989. Peak radiance for a blackbody with these characteristics occurs in the SWIR at $150.8 \mu\text{W cm}^{-2} \text{sr}^{-1} \text{nm}^{-1}$ when accounting for the modeled atmospheric conditions for the Simi Fire AVIRIS scene. An ideal SWIR saturation threshold for HypsIRI VSWIR would be at least higher than this radiance value, although practical considerations for measuring reflected solar radiance likely require a much lower saturation threshold. It should be noted that this threshold was calculated from unsaturated bands. A higher threshold might have resulted if data from spectra completely saturated throughout the SWIR could have been analyzed, although these hot spots would also likely have low fractional areas within a 60 m pixel.

Spectral averaging with spatial resampling also had an effect on background endmember modeling. Variability of land cover was reduced in coarser resolution images when compared to finer resolutions. The broad land cover characteristics did remain consistent across all spatial resolutions, and confusion between widely different land cover types (e.g., oak forest vs. soil/rock) was rare, even at the coarsest spatial resolutions. Classification accuracies were not assessed due to the lack of *in situ* data for the areas within each AVIRIS scene. Additionally, this study did not examine the use of endmembers retrieved from coarser spatial resolutions in the MESMA modeling. Schaaf et al. (2011) found that selection of endmembers for MESMA from finer spatial resolution images resulted in higher classification accuracies in coarser resolution images. Lower accuracy may therefore be expected when modeling with endmembers selected from resolutions closer to 60 m, but this remains to be tested, since no pre-fire *in situ* reference data existed for the scenes used in this study.

6. Conclusions

This study examined the performance of HFDI fire detection and MESMA temperature modeling across multiple spatial resolutions for four AVIRIS scenes containing actively burning wildfires. A saturation mask was used to ensure that saturated bands would not distort radiance values in the spatially aggregated data. Spatial aggregation was compared to a more realistic Gaussian point spread function at 60.0 m resolution. The two resampling techniques were found to produce similar radiance values, although Gaussian resampling resulted in additional fire area modeled at lower temperatures. Modeling results supported the viability of hyperspectral fire detection and effective temperature modeling using data with HypsIRI-like spatial resolutions. Temperature distributions were similar across a wide range of spatial resolutions. However, coarser spatial resolution hyperspectral data, such as those collected by the future HypsIRI VSWIR sensor, may be expected to model more fire area at lower

temperatures when compared against simultaneously acquired higher spatial resolution data. Adjustments to saturation thresholds in SWIR bands could provide additional unsaturated bands for more effective retrieval of fire properties.

The proposed HypsIRI mission promises vastly superior spatial and temporal coverage compared to AVIRIS, providing global coverage multiple times per year. Temporal analysis could allow linking of retrieved fire properties with impacts on soil and post-fire vegetation succession, thus improving understanding of fire-ecosystem processes. Data from the HypsIRI multispectral thermal infrared imager (TIR) will be acquired simultaneously with VSWIR data at 60 m spatial resolution. The TIR sensor will include a $4 \mu\text{m}$ band that is spectrally similar to those currently used to produce MODIS fire detection and fire radiative power products. HypsIRI's hyperspectral VSWIR and multispectral TIR sensors should provide a powerful combination for measurement of fire radiative properties.

Acknowledgments

We would like to acknowledge Sarah Lundeen, Robert Green, and the NASA-JPL AVIRIS team for providing the AVIRIS data used in this paper.

References

- Amici, S., Wooster, M. J., & Piscini, A. (2011). Multi-resolution spectral analysis of wild-fire potassium emission signatures using laboratory, airborne and spaceborne remote sensing. *Remote Sensing of Environment*, 115, 1811–1823.
- Anderson, M. C., Kustas, W. P., & Norman, J. M. (2007). Upscaling flux observations from local to continental scales using thermal remote sensing. *Agronomy Journal*, 99, 240–254.
- Berk, A., Bernstein, L. S., & Robertson, D. C. (1989). *MODTRAN: A moderate resolution model for LOWTRAN7*, AFGL-TR-89-0122. MA: Hanscom Air Force Base.
- Bian, L. (1997). Multiscale nature of spatial data in scaling up environmental models. In D. A. Quattrochi, & M. F. Goodchild (Eds.), *Scale in remote sensing and GIS* (pp. 13–26). Boca Raton, FL: Lewis Publishers.
- Boardman, J. W. (1999). Precision geocoding of low altitude AVIRIS data: Lessons learned in 1998. *Summaries of the eighth JPL Airborne Earth Science Workshop*, 99 – 17 (pp. 63–68). Pasadena: Jet Propulsion Laboratory, JPL Publication.
- California Department of Forestry and Fire Protection (2007). Incident information. http://cdfdata.fire.ca.gov/incidents/incidents_details_info?incident_id=190
- Cohen, J. (1960). A coefficient of agreement for nominal scales. *Educational and Psychological Measurement*, 20, 37–46.
- Csiszar, I., Morisette, J., & Giglio, L. (2006). Validation of active fire detection from moderate resolution satellite sensors: The MODIS example in Northern Eurasia. *IEEE Transactions on Geoscience and Remote Sensing*, 44, 1757–1764.
- Csiszar, I., & Schroeder, W. (2008). Short-term observations of the temporal development of active fires from consecutive same-day ETM+ and ASTER imagery in the Amazon: Implications for active fire product validation. *IEEE Journal of Selected Topics in Applied Earth Observations and Remote Sensing*, 1, 248–253.
- Dennison, P. E. (2006). Fire detection in imaging spectrometer data using atmospheric carbon dioxide absorption. *International Journal of Remote Sensing*, 27(14), 3049–3055.
- Dennison, P. E., Charoensiri, K., Roberts, D. A., Peterson, S. H., & Green, R. O. (2006). Wildfire temperature and land cover modeling using hyperspectral data. *Remote Sensing of Environment*, 100, 212–222.
- Dennison, P. E., & Matheson, D. S. (2011). Comparison of fire temperature and fractional area modeled from SWIR, MIR, and TIR multispectral and SWIR hyperspectral airborne data. *Remote Sensing of Environment*, 115, 876–886.
- Dennison, P. E., & Roberts, D. A. (2009). Daytime fire detection using airborne hyperspectral data. *Remote Sensing of Environment*, 113, 1646–1657.
- Dennison, P. E., Roberts, D. A., Thorgusen, S. R., Regelbrugge, J. C., Weise, D., & Lee, C. (2003). Modeling seasonal changes in live fuel moisture and equivalent water thickness using a cumulative water balance index. *Remote Sensing of Environment*, 88, 442–452.
- Dozier, J. (1981). A method for satellite identification of surface temperature fields of subpixel resolution. *Remote Sensing of Environment*, 11, 221–229.
- Eckmann, T. C., Roberts, D. A., & Still, C. J. (2008). Using multiple endmember spectral mixture analysis to retrieve subpixel fire properties from MODIS. *Remote Sensing of Environment*, 112, 3773–3783.
- Eckmann, T. C., Roberts, D. A., & Still, C. J. (2009). Estimating subpixel fire sizes and temperatures from ASTER using multiple endmember spectral mixture analysis. *International Journal of Remote Sensing*, 30(22), 5851–5864.
- Eckmann, T. C., Still, C. J., Roberts, D. A., & Michaelsen, J. C. (2010). Variations in subpixel fire properties with season and land cover in Southern Africa. *Earth Interactions*, 14–006.
- Giglio, L., & Kendall, J. D. (2001). Application of the Dozier retrieval to wildfire characterization: A sensitivity analysis. *Remote Sensing of Environment*, 77(1), 34–49.

- Green, R. O. (1996). Estimation of biomass fire temperature and areal extent from calibrated AVIRIS spectra. *Summaries of the Sixth Annual JPL Airborne Earth Science Workshop, 96-4(1)*. (pp. 105–113)Pasadena: Jet Propulsion Laboratory.
- Kokaly, R. F., Rockwell, B. W., Haire, S. L., & King, T. V. V. (2007). Characterization of post-fire surface covers, soils, and burn severity at the Cerro Grande Fire, New Mexico, using hyperspectral and multispectral remote sensing. *Remote Sensing of Environment, 106*, 305–325.
- Kushida, K. (2010). Detection of active wildfires using multitemporal MODIS images. *IEEE Geoscience and Remote Sensing Letters, 7*, 301–305.
- Lee, D., & Sallee, G. (1970). A method of measuring shape. *Geographical Review, 60*, 555–563.
- Lentile, L. B., Holden, Z. A., Smith, A. M. S., Falkowski, M. J., Hudak, A. T., Morgan, P., et al. (2006). Remote sensing techniques to assess active fire and post-fire effects. *International Journal of Wildland Fire, 15*, 319–345.
- Lewis, S. A., Lentile, L. B., Hudak, A. T., Robichaud, P. R., Morgan, P., & Bobbitt, M. J. (2007). Mapping ground cover using hyperspectral remote sensing after the 2003 Simi and Old wildfires in southern California. *Fire Ecology, 3*, 109–128.
- Massey, F. J. (1951). The Kolmogorov–Smirnov test for goodness of fit. *Journal of the American Statistical Association, 46(253)*, 68–78.
- Morisette, J. T., Giglio, L., Csiszar, I., & Justice, C. O. (2005a). Validation of the MODIS active fire product over Southern Africa with ASTER data. *International Journal of Remote Sensing, 26*, 4239–4264.
- Morisette, J. T., Giglio, L., Csiszar, I., Setzer, A., Schroeder, W., Morton, D., et al. (2005b). Validation of MODIS active fire detection products derived from two algorithms. *Earth Interactions, 9(9)*, 1–25.
- National Research Council Committee on Earth Science and Applications from Space (2007). *Earth science and applications from space: National imperatives for the next decade and beyond*. Washington, D.C.: National Academies Press.
- Nelson, M. D., McRoberts, R. E., Holden, G. R., & Bauer, M. E. (2009). Effects of satellite image spatial aggregation and resolution on estimates of forest land area. *International Journal of Remote Sensing, 30(8)*, 1913–1940.
- Rahman, A. F., Gamon, J. A., Sims, D. A., & Schmidt, M. (2003). Optimum pixel size for hyperspectral studies of ecosystem function in southern California chaparral and grassland. *Remote Sensing of Environment, 84*, 192–207.
- Riaño, D., Chuvieco, E., Ustin, S., Zomer, R., Dennison, P., Roberts, D., et al. (2002). Assessment of the vegetation regeneration after fire through the multitemporal analysis of AVIRIS images in the Santa Monica Mountains. *Remote Sensing of Environment, 79*, 60–71.
- Roberts, D. A., Gardner, M., Church, R., Ustin, S., Scheer, G., & Green, R. O. (1998). Mapping chaparral in the Santa Monica Mountains using multiple endmember spectral mixture models. *Remote Sensing of Environment, 65*, 267–279.
- Schaaf, A. N., Dennison, P. E., Fryer, G. K., Roth, K. L., & Roberts, D. A. (2011). Using hyperspectral data to classify vegetation at the plant functional type-level in mountain terrain at three spatial resolutions. *GIScience and Remote Sensing, 48*, 324–344.
- Schroeder, W., Prins, E., Giglio, L., Csiszar, I., Schmidt, C., Morisette, J., et al. (2008). Validation of GOES and MODIS active fire detection products using ASTER and ETM+ data. *Remote Sensing of Environment, 112*, 2711–2726.
- Varga, T. A., & Asner, G. P. (2008). Hyperspectral and lidar remote sensing of fire fuels in Hawaii Volcanoes National Park. *Ecological Applications, 18*, 613–623.
- Vodacek, A., Kremens, R. L., Fordham, A. J., Vangorden, S. C., Luisi, D., Schott, J. R., et al. (2002). Remote optical detection of biomass burning using a potassium emission signature. *International Journal of Remote Sensing, 13*, 2721–2726.
- Walsh, S. J., Moody, A., Allen, T. R., & Brown, D. G. (1997). In D. A. Quattrochi, & M. F. Goodchild (Eds.), *Scale in remote sensing and GIS (27–56)*. Boca Raton, FL: Lewis Publishers.